

# UC Irvine

## UC Irvine Previously Published Works

### Title

Spectroscopic analysis of the sum-frequency response of the carbon–hydrogen stretching modes in collagen type I

### Permalink

<https://escholarship.org/uc/item/362724b4>

### Journal

The Journal of Chemical Physics, 160(18)

### ISSN

0021-9606

### Authors

Luna Palacios, Yryx Y

Khandani, Salile

Garcia, Evan P

et al.

### Publication Date

2024-05-14

### DOI

10.1063/5.0205685

### Copyright Information








This work is made available under the terms of a Creative Commons Attribution License, available at <https://creativecommons.org/licenses/by/4.0/>

Peer reviewed

RESEARCH ARTICLE | MAY 08 2024

## Spectroscopic analysis of the sum-frequency response of the carbon–hydrogen stretching modes in collagen type I

Special Collection: [Festschrift in honor of Yuen-Ron Shen](#)

Yryx Y. Luna Palacios ; Salile Khandani; Evan P. Garcia; Anabel Chen ; Siyang Wang ; Khokan Roy; David Knez ; Do A. Kim; Israel Rocha-Mendoza ; Eric O. Potma  



*J. Chem. Phys.* 160, 185101 (2024)

<https://doi.org/10.1063/5.0205685>



### Articles You May Be Interested In

Infrared harmonic features of collagen models at B3LYP-D3: From amide bands to the THz region

*J. Chem. Phys.* (August 2021)

Quantitatively linking collagen alteration and epithelial tumor progression by second harmonic generation microscopy

*Appl. Phys. Lett.* (May 2010)

Room temperature TiO<sub>2</sub> atomic layer deposition on collagen membrane from a titanium alkylamide precursor

*J. Vac. Sci. Technol. A* (December 2016)

05 February 2025 22:17:45



The Journal of Chemical Physics

## Special Topics Open for Submissions

[Learn More](#)

# Spectroscopic analysis of the sum-frequency response of the carbon–hydrogen stretching modes in collagen type I

Cite as: J. Chem. Phys. 160, 185101 (2024); doi: 10.1063/5.0205685

Submitted: 27 February 2024 • Accepted: 22 April 2024 •

Published Online: 8 May 2024



View Online



Export Citation



CrossMark

Yryx Y. Luna Palacios,<sup>1</sup>  Salile Khandani,<sup>2</sup> Evan P. Garcia,<sup>1</sup> Anabel Chen,<sup>1</sup>  Siyang Wang,<sup>1</sup>  Khokan Roy,<sup>1</sup> David Knez,<sup>1</sup>  Do A. Kim,<sup>2</sup> Israel Rocha-Mendoza,<sup>3</sup>  and Eric O. Potma<sup>1,2,a)</sup> 

## AFFILIATIONS

<sup>1</sup>Department of Chemistry, University of California at Irvine, Irvine, California 92697-2025, USA

<sup>2</sup>Department of Biomedical Engineering, University of California at Irvine, Irvine, California 92697-2025, USA

<sup>3</sup>Centro de Investigación Científica y de Educación Superior de Ensenada (CICESE), Carretera Ensenada-Tijuana, No. 3918, Zona Playitas, Ensenada 22860, Mexico

**Note:** This paper is part of the JCP Festschrift in honor of Yuen-Ron Shen.

**a)** Author to whom correspondence should be addressed: [epotma@uci.edu](mailto:epotma@uci.edu)

## ABSTRACT

We studied the origin of the vibrational signatures in the sum-frequency generation (SFG) spectrum of fibrillar collagen type I in the carbon–hydrogen stretching regime. For this purpose, we developed an all-reflective, laser-scanning SFG microscope with minimum chromatic aberrations and excellent retention of the polarization state of the incident beams. We performed detailed SFG measurements of aligned collagen fibers obtained from rat tail tendon, enabling the characterization of the magnitude and polarization-orientation dependence of individual tensor elements  $X_{ijk}^{(2)}$  of collagen's nonlinear susceptibility. Using the three-dimensional atomic positions derived from published crystallographic data of collagen type I, we simulated its  $X_{ijk}^{(2)}$  elements for the methylene stretching vibration and compared the predicted response with the experimental results. Our analysis revealed that the carbon–hydrogen stretching range of the SFG spectrum is dominated by symmetric stretching modes of methylene bridge groups on the pyrrolidine rings of the proline and hydroxyproline residues, giving rise to a dominant peak near  $2942\text{ cm}^{-1}$  and a shoulder at  $2917\text{ cm}^{-1}$ . Weak asymmetric stretches of the methylene bridge group of glycine are observed in the region near  $2870\text{ cm}^{-1}$ , whereas asymmetric  $\text{CH}_2$ -stretching modes on the pyrrolidine rings are found in the  $2980$  to  $3030\text{ cm}^{-1}$  range. These findings help predict the protein's nonlinear optical properties from its crystal structure, thus establishing a connection between the protein structure and SFG spectroscopic measurements.

Published under an exclusive license by AIP Publishing. <https://doi.org/10.1063/5.0205685>

## I. INTRODUCTION

Collagen encompasses a group of extracellular matrix proteins that are pivotal for the structural and mechanical properties of connective tissues as well as for cell adhesion, migration, and proliferation. Collagen type I, which constitutes the primary structural framework in connective tissues, features a distinct triple-helical structure with a repeating Gly–X–Y motif, where X and Y commonly represent the proline or hydroxyproline amino acid residues.<sup>1,2</sup> The triple-helix structure assigns structural non-centrosymmetry to the collagen I molecule. This property is maintained in the higher-order hierarchical structures of collagen, including its fibrils and fibers.

Because of this non-centrosymmetry, collagen type I exhibits a non-vanishing second-order susceptibility  $[\chi^{(2)}]$ , which has made it a popular target for the second-harmonic generation (SHG) microscopy technique.<sup>3</sup> The unique imaging properties of SHG microscopy have made it possible to not only visualize the distribution of collagen type I in biological tissues but also extract information about its fibrillar orientation,<sup>4–7</sup> polar alignment,<sup>8,9</sup> backbone structure,<sup>10–12</sup> and density.<sup>13,14</sup>

Although SHG microscopy has become synonymous with label-free imaging of collagen, the technique struggles with linking local chemical properties of molecular collagen to the structural properties of fibrillar or fibrous collagen on a macroscopic level. The

SHG technique is commonly performed under non-resonant spectroscopic conditions, thus excluding the possibility of tuning into specific resonances that correspond to collagen's chemical structure. Sum-frequency generation (SFG) is related to SHG, but because it can be performed under vibrationally resonant conditions, it can be used to probe molecular spectroscopic information that is not easily accessible with SHG approaches.<sup>15,16</sup> Vibrationally sensitive SFG microscopy has emerged as a viable alternative to SHG imaging when spectroscopic sensitivity is required.<sup>17–19</sup> SFG microscopy has been used successfully to study collagen I derived from tissue,<sup>20</sup> and phase-sensitive studies have revealed relevant information about fibrillar orientation within fibrous collagen.<sup>21,22</sup>

Most SFG imaging studies of collagen type I to date have been carried out in the spectral range that corresponds to the fundamental stretching vibrations of carbon–hydrogen bonds. The SFG spectroscopic measurements in this range generally reveal a broad-band structure with a single maximum near  $2940\text{ cm}^{-1}$ .<sup>23–25</sup> Based on the chemical structure of collagen type I, which is rich in methylene groups and relatively devoid of methyl groups, the methylene stretching vibrations can be identified as the likely source of the observed SFG signatures. The vibrational energy that corresponds to  $2940\text{ cm}^{-1}$  is, however, much higher than what is commonly observed for methylene modes in aliphatic structures, which exhibit symmetric  $\nu_s$  ( $\text{CH}_2$ ) stretches in the  $2835\text{--}2865\text{ cm}^{-1}$  range and asymmetric  $\nu_{as}$  ( $\text{CH}_2$ ) stretches in the  $2870\text{--}2910\text{ cm}^{-1}$  spectral window. The band structure of the  $\text{CH}_2$  stretching modes is often broadened by the presence of Fermi resonances, resulting from the mixing of the overtone of symmetric bending modes with the symmetric stretching mode, which can complicate band assignments. For these reasons, collagen's SFG spectrum in the carbon–hydrogen stretching range is not well understood, a fact that has limited a deeper analysis of spectroscopic SFG imaging data.

It has been hypothesized that the main peak near  $2940\text{ cm}^{-1}$  is the result of a Fermi resonance, which is supported by spectroscopic SFG data that suggest that this spectroscopic feature corresponds to a symmetric mode.<sup>25</sup> This notion also appears to be in line with a polarization-resolved SFG imaging study in tendon tissue.<sup>20</sup> Nonetheless, a full analysis of mode symmetries across the band has never been performed, the role of asymmetric modes remains unclear, and a comparison with linear Raman and infrared (IR) absorption spectroscopic data has not yet been completed. Consequently, the correct band assignments in this spectroscopically important region remain inconclusive, complicating a more complete structural analysis of collagen.

In this work, we perform detailed SFG microscopic measurements of collagen type I fibrils derived from rat tail tendon tissue. This work expands on previous studies in several key aspects. First, by simulating the SFG response with the aid of data extracted from the protein data bank (PDB), we show that polarization-sensitive measurements can conclusively identify the symmetry of a given spectral mode of collagen. Second, we have built an all-reflective SFG microscope that suppresses aberrations to the polarization state of the incident optical fields, allowing measurements of individual tensor elements of  $\chi^{(2)}$  with unprecedented precision. Third, we analyze the SFG imaging results in the context of collagen's linear Raman and IR absorption spectra and provide density functional theory simulations of relevant amino acid residues to aid in the band assignments. Based on this approach, we suggest new assignments

of collagen's SFG spectroscopic features in the  $\text{CH}_2$  stretching range.

## II. MATERIALS AND METHODS

### A. Sample

The collagen type I samples were extracted from fresh rat tail tendon. The excised segments were gently flattened to achieve tissue slices of  $\sim 100\text{ }\mu\text{m}$  thickness and sandwiched between two cover slides in a hydrated state. Borosilicate no. 1 slides were used for this purpose, which, despite their small but non-negligible IR-absorption, improved the experimental workflow.

### B. Raman and FTIR spectrum

The Fourier transform IR (FTIR) spectra of extracted collagen tissue samples were collected in attenuated total reflectance (ATR) mode on an FTIR spectrometer (Jasco 4100 FTIR). The Raman spectra were acquired on a confocal Raman microscope (InVia, Renishaw), utilizing a  $0.75$  numerical aperture (NA) dry objective lens and an excitation wavelength of  $532\text{ nm}$ . The Raman spectra were measured in reflection mode, with the sample positioned between two cover slips.

### C. Reflective SFG microscope

The polarization-sensitive SFG measurements were carried out on an all-reflective SFG microscope. A schematic representation of the setup is shown in Fig. 1(a). The system uses a picosecond,  $1031\text{ nm}$   $\text{Yb}^{3+}$ -fiber laser source (aeroPULSE, NKT Photonics), which produced  $6\text{ ps}$  pulses at a repetition rate of  $76\text{ MHz}$ . The near IR output at  $1031\text{ nm}$  ( $9708\text{ cm}^{-1}$ ) served as the pump source for a mid-IR optical parametric oscillator (OPO, Levante IR, A.P.E. Berlin). The OPO signal output was tuned from  $2810$  to  $3030\text{ cm}^{-1}$  ( $3556$  to  $3300\text{ nm}$ ) and provided the  $\omega_1$  field in the SFG process. The  $\omega_2$  interaction in the SFG process was provided by the residual  $1031\text{ nm}$  beam. Both beams were spatially filtered, and the linear polarization state of each incident beam was controlled by a polarizer and a half-wave plate. After collinear recombination on a dichroic mirror, both beams were directed toward galvanometric mirrors (galvo) and a reflective relay system.

The reflective relay images the plane intermediate between the two galvanometric mirrors onto the back aperture plane of the reflective objective lens. Reflective optics were chosen to mitigate chromatic aberrations and dispersion effects across a broad range of frequencies, as well as to minimize the depolarization effects of the incident beams. The reflective relay system comprised five mirrors. M1 was a flat mirror that redirected the excitation beams from the galvo scanner to concave mirror M2 ( $f = 500\text{ mm}$ ), which subsequently steered the beams onto concave mirror M3 ( $f = 1500\text{ mm}$ ). M3 then reflected the input beams to concave mirror M4 ( $f = 400\text{ mm}$ ), followed by a flat mirror M5 that guided the beams into the microscope frame. The reflective relay was optimized in ZEMAX and configured for minimal aberrations and diffraction-limited performance. The overall magnification of the relay system is  $1.1$ .

The beams were focused onto the sample by a Schwarzschild–Cassegrain objective (model 5007, Beck), which has a numerical aperture of  $0.65$ . The SFG signal is collected in the

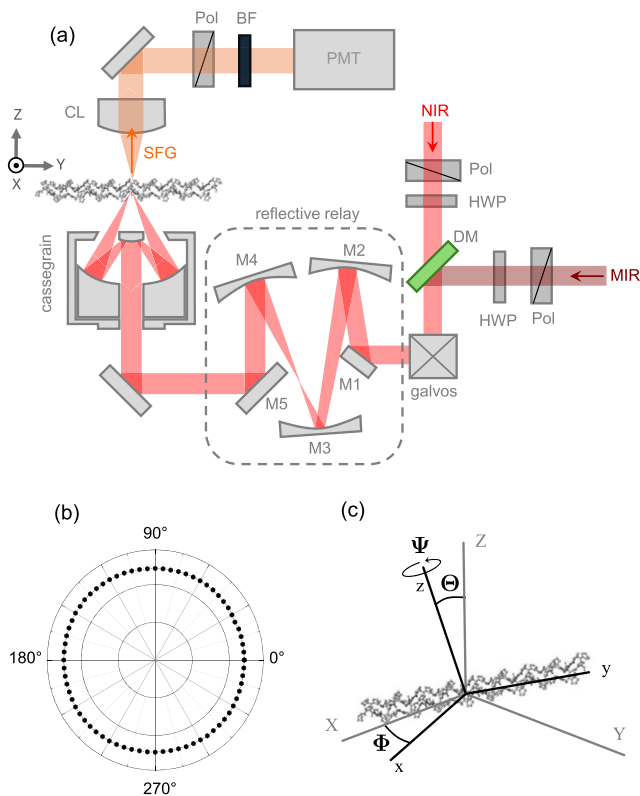


**FIG. 1.** Experimental configuration. (a) All-reflective polarization-sensitive SFG microscope. The (linear) polarization orientation for the mid-IR infrared ( $\omega_1$ ) and near-IR ( $\omega_2$ ) beams are controlled by a half-wave plate (HWP). The beams are combined on a dichroic mirror (DM) and directed toward a galvanometric scanner (galvos), followed by a reflective relay system. The beams are focused onto the sample by a 0.65 NA reflective objective (Schwarzschild-Cassegrain). The SFG signal is collected by a condenser lens (CL), analyzed by a linear polarizer (Pol), filtered by a bandpass filter (BF), and detected by a photon counting head (PMT). M1 and M5 are flat mirrors. M2 ( $f = 500$  mm), M3 ( $f = 1500$  mm), and M4 ( $f = 400$  mm) are concave mirrors. The beam angles are not to scale. (b) Throughput of the 1031 nm beam through the optical system for different orientations of the linear input polarization and analyzer detection angle. (c) Alignment of the collagen frame ( $x, y, z$ ) with the laboratory frame ( $X, Y, Z$ ), defined by the Euler angles ( $\Phi, \Theta, \Psi$ ).

forward direction by a refractive condenser lens, passing through a bandpass filter (780–800 nm pass band) and a linear polarizer (analyzer) before detection by a photon counting head (H16721-50, Hamamatsu). Figure 1(b) shows the transmission of the 1031 nm beam through the optical system, for different polar angles of the linear polarization, by rotating the half-wave plate, polarizer, and analyzer at the appropriate angle. It can be seen that there are no detectable depolarization effects as the beams pass through the full optical imaging system. The excellent polarization properties of the all-reflective optical system ensure the accuracy of the polarization-sensitive SFG measurements reported here. For the imaging experiments, the long axis of the collagen fibers, which was visible by eye upon inspection in the microscope, was aligned along the Y-axis of the laboratory frame, when all Euler angles are zero;

see Fig. 1(c). For the images used in this work, the uncertainty in the fibrillar alignment is  $\Delta\Phi = 4.0^\circ$  as determined from a Fourier analysis of the images.

#### D. Computational framework

We developed a computational framework for simulating the expected SFG response from the methylene stretching modes in fibrillar collagen type I. For this purpose, we used the crystal structure of collagen type I from the PDB<sup>26</sup> for extracting atomic coordinates and determining the signal contributions from individual methylene bridge groups (referred to as the methylene group from here on) in the fibrillar structure.

The response from an individual methylene group is described by its hyperpolarizability tensor, which has the elements  $\beta_{abc}$ , as defined in the molecular frame ( $a, b, c$ ). The indices of the hyperpolarizability correspond, from right to left, to the interaction with a given field component of  $\omega_1, \omega_2$ , and  $\omega_3 = \omega_1 + \omega_2$ , respectively. The molecular axes of the  $\text{CH}_2$  oscillator are chosen in the same fashion as in Wang *et al.*,<sup>27</sup> where the  $c$ -axis is bisecting the H–C–H angle and the  $ac$ -plane includes the H–C–H bonds. We assume the  $C_{2v}$  symmetry for the H–C–H unit, in which case there are only seven non-zero elements of the hyperpolarizability, namely  $\beta_{aac}, \beta_{bbc}, \beta_{ccc}, \beta_{aca} = \beta_{caa},$  and  $\beta_{bcb} = \beta_{cbb}$ , where the first three elements correspond to the symmetric mode and the last four elements correspond to the asymmetric mode. Note that in the case of distortions due to vibrational coupling, the strict  $C_{2v}$  symmetry may no longer be valid for certain methylene groups in the fibrillar structure, in which case some of the otherwise zero-valued tensor elements may become finite.<sup>28</sup> In this work, we use the bond polarizability derivative model to obtain the estimates of the non-zero tensor elements.<sup>29,30</sup> Despite its approximate nature, this model has been shown to provide reasonable hyperpolarizability values for the  $\text{CH}_2$  stretching vibrations, in particular for the symmetric stretching mode.<sup>27,31</sup>

Once the elements of the hyperpolarizability tensor are defined, the second-order optical response of a segment of collagen's triple helix can be determined by coherently summing the non-zero contributions of the individual methylene groups. The collagen molecule is defined in the supramolecular frame ( $x, y, z$ ), and its long axis is placed along the  $y$ -axis. The Euler rotations over ( $\phi, \theta, \psi$ ), as defined in Fig. S1 of the supplementary material, determine the projections of the tensor elements of each methylene group onto the axis of the supramolecular frame. The response of the collagen segment is now described by its second-order susceptibility, computed as

$$\chi_{ijk}^{(2)} = N_m \sum_{abc} \langle R_{ia} R_{jb} R_{kc} \rangle \beta_{abc}, \quad (1)$$

where  $N_m$  is the number density of the methylene monomers (in units of  $\text{m}^{-3}$ ), the subindex  $ijk$  indicates the Cartesian polarization component for the fields  $\omega_3, \omega_2$ , and  $\omega_1$  (i.e., SFG, NIR, and MIR), respectively.  $R_{ia} R_{jb} R_{kc}$  represent the elements of the rotation matrix for each of the field interactions, and the brackets indicate the orientational average. Given that the Euler angles of each methylene monomer can be determined from the crystal structure, Eq. (1) allows for the computation of all elements of  $\chi^{(2)}$  in the supramolecular frame without further approximations. Nonetheless, it is also useful to relate the computational results to analytical estimates when assuming that collagen exhibits  $C_\infty$  symmetry with respect to

the fibrillar axis. Under this common assumption, we expect seven non-zero achiral tensor elements ( $\chi_{yyy}^{(2)}, \chi_{yzz}^{(2)} = \chi_{yxx}^{(2)}, \chi_{zzy}^{(2)} = \chi_{xxy}^{(2)}, \chi_{zyz}^{(2)} = \chi_{xyx}^{(2)}$ ) and six non-zero chiral tensor elements ( $\chi_{zxy}^{(2)} = -\chi_{xzy}^{(2)}, \chi_{xyx}^{(2)} = -\chi_{zyx}^{(2)}, \chi_{yzz}^{(2)} = \chi_{yzz}^{(2)}$ ) that contribute to the SFG signal of fibrillar systems.<sup>25,32</sup>

In the actual SFG imaging experiments, the collagen fibrils assume a certain orientation in the laboratory frame ( $X, Y, Z$ ), as defined by the Euler angles ( $\Phi, \Theta, \Psi$ ). In general, collagen's response in the laboratory frame can be obtained from the following relation:

$$\chi_{IJK}^{(2)} = N_s \sum_{ijk} \langle R_{Ii} R_{Jj} R_{Kk} \rangle \chi_{ijk}^{(2)}, \quad (2)$$

where  $\chi_{IJK}^{(2)}$  are the elements of the nonlinear susceptibility in the laboratory frame,  $N_s$  is the number of collagen molecules that contribute to the volume element described by  $\chi_{IJK}^{(2)}$ , and  $R_{Ii} R_{Jj} R_{Kk}$  are rotations over ( $\Phi, \Theta, \Psi$ ) for each of the field interactions. In the experiments, we have aligned the fibrillar axis along the  $Y$ -axis so that the collagen supramolecular ( $x, y, z$ ) frame aligns with the laboratory frame ( $X, Y, Z$ ), whereas the polarization direction of the incident fields is rotated relative to the  $Y$ -axis in the lateral plane.

The computations are performed in MATLAB, based on the following procedure: (1) extraction of atomic coordinates associated with each methylene group from the crystal structure, (2) calculation of the Euler angles ( $\phi, \theta, \psi$ ) for each  $\text{CH}_2$  monomer, (3) calculation of the  $\chi_{ijk}^{(2)}$  tensor elements using Eq. (1), and (4) determination of the  $\chi_{IJK}^{(2)}$  dependence on the orientation angle  $\Phi$  utilizing Eq. (2). In this work, we are concerned with the sample's nonlinear optical response per volume element, in which case  $\chi_{ijk}^{(2)}$  is expressed in units of  $\text{m/V}$  (SI units).

### E. Density functional theory calculations

The density functional theory (DFT) simulations were performed in the GaussView 6.0.16 software, using the PBEPBE method and the tzvp basis set. In all calculations, the compound is assumed to be in the gas phase. The calculated Raman lines are displayed as Lorentzian line shapes with a full width at half maximum of  $20 \text{ cm}^{-1}$ .

## III. RESULTS

### A. Simulated magnitude and polarization dependence of SFG tensor elements

We performed simulations of the SFG signal to ascertain the sensitivity of polarization-resolved measurements to the symmetry properties of the methylene stretching modes. As detailed in Sec. II D, we used the atomic coordinate information from collagen type I published in the PDB to simulate the contribution of the methylene group's symmetric and asymmetric vibrations to the SFG signal. Our calculations encompassed all 27 tensor elements of the supramolecular tensor elements  $\chi_{ijk}^{(2)}$ . The simulations assumed that collagen's primary axis  $y$  was aligned with the  $Y$ -axis of the laboratory frame; see Fig. 1(c). The detailed results for these tensor elements are provided in the supplementary material, including analyses for a methylene monomer and the selected segment of collagen type I.

We note that our calculations revealed substantial values for the chiral elements in collagen type I even though the individual monomers are considered to be achiral responders. The presence of chirality at the supramolecular level can be attributed to the specific three-dimensional orientation distribution of the (achiral) monomers in a uniaxial system (such as fibrillar systems), which, after orientational averaging, yields non-zero chiral elements of the SFG nonlinear susceptibility tensor.<sup>33–35</sup> Nonetheless, in our experiments, the chiral tensor elements were not expected to contribute significantly to the measured SFG signal. Because the collagen fibers were predominantly aligned in the  $XY$ -plane and the beams incident on the reflective objective exhibited only transverse polarization components, tensor elements with  $Z$ -indices were not efficiently probed in the experiments reported here, which excludes a prominent role for the chiral tensor elements. Consequently, we expect that the measured SFG signal is primarily dictated by the achiral elements  $\chi_{yyy}^{(2)}, \chi_{xxy}^{(2)}, \chi_{yxx}^{(2)}$ , and  $\chi_{xyx}^{(2)}$ .

Figure 2 shows the simulated values of selected elements  $\chi_{ijk}^{(2)}$  computed for the 155 methylene groups in a segment of the triple helix of human collagen type I. It can be seen that the largest molecular tensor elements for the symmetric modes are  $\chi_{xxy}^{(2)}$  and  $\chi_{yyy}^{(2)}$ , of which both are negative. In contrast, the symmetric contributions to  $\chi_{yxx}^{(2)}$  and  $\chi_{xyx}^{(2)}$  are considerably weaker. The overall magnitude of the simulated vibrationally resonant tensor elements is in the  $\text{pm/V}$  range, slightly higher than the values reported for the non-resonant nonlinear susceptibility made with the SHG technique.<sup>36,37</sup> Note that different elements may differ in sign and that they may thus either constructively or destructively add to the coherent sum in a given polarization detection channel.

In the case of asymmetric modes,  $\chi_{xyx}^{(2)}$  exhibits the highest value among the achiral elements, suggesting that methylene asymmetric modes require an  $\omega_1$  component of the incident field normal to the principal  $y$ -axis, and the SFG signal is mostly linearly polarized along  $x$  [since the contribution of  $\chi_{yxx}^{(2)}$  is minor]. Consequently, the asymmetric mode contributes only moderately to the achiral elements  $\chi_{yyy}^{(2)}$  and  $\chi_{xxy}^{(2)}$ , which are dominant for the symmetric mode. We note that the elements that are predicted to vanish under perfect  $C_\infty$  symmetry are generally non-vanishing in the simulations based on the

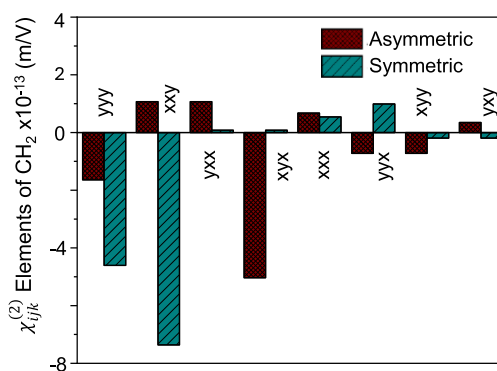


FIG. 2. Magnitude of selected achiral  $\chi_{ijk}^{(2)}$  elements for the contribution of methylene stretching vibrations in collagen type I.



actual crystal structure. This includes the elements  $\chi_{xxx}^{(2)}$ ,  $\chi_{yyx}^{(2)}$ ,  $\chi_{xyy}^{(2)}$ , and  $\chi_{yxy}^{(2)}$ , which are relatively small but non-zero, as shown in Fig. 2. Such can be expected, as the collagen crystal structure used in the simulation comprises a finite number of methylene groups and does not represent a system with perfect cylindrical symmetry, even after spatial averaging. Nonetheless, the elements that are expected to be nonzero under  $C_\infty$  symmetry are, on average, found to be about one order of magnitude higher than the elements that are expected to be zero. This observation indicates that the relatively short segment of collagen still exhibits symmetry properties that roughly mimic those of a system with true  $C_\infty$  symmetry.

Figure 3 compares the magnitude of the squared amplitude  $|\chi_{ijk}^{(2)}|^2$  of the tensor elements  $\chi_{yyy}^{(2)}$ ,  $\chi_{xxy}^{(2)}$ ,  $\chi_{xyx}^{(2)}$ ,  $\chi_{xyy}^{(2)}$ , and  $\chi_{xyx}^{(2)}$  for both symmetric and asymmetric modes, represented in the form of a Lorentzian line shape for easy comparison. Because the symmetric and asymmetric modes contribute differently to the various tensor elements, they can be discriminated via polarization-resolved measurements.

We considered polarization-resolved experiments in which both input beams are initially linearly polarized in the same direction along the  $Y$ -axis of the sample plane. With the collagen fibrils oriented parallel to the same  $Y$ -axis, the laboratory and supramolecular frame are aligned so that a measurement of the  $\chi_{IJK}^{(2)}$  element in the laboratory frame reveals  $\chi_{ijk}^{(2)}$  in the supramolecular frame with  $I \rightarrow i$ ,  $J \rightarrow j$ , and  $K \rightarrow k$ . For instance, a  $\chi_{YYY}^{(2)}$  measurement probes the  $\chi_{yyy}^{(2)}$  properties of the supramolecular structure. However, this is no longer the case when the polarization directions of the incident beams are simultaneously rotated within the transverse ( $XY$ ) plane, as a  $\chi_{YYY}^{(2)}$  measurement now contains contributions from other non-zero elements  $\chi_{ijk}^{(2)}$ . Upon a full polarization rotation over

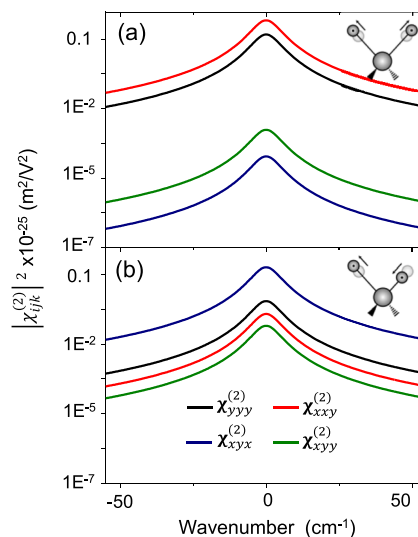


FIG. 3. Squared amplitude  $|\chi_{ijk}^{(2)}|^2$  of the tensor elements  $\chi_{yyy}^{(2)}$ ,  $\chi_{xxy}^{(2)}$ ,  $\chi_{xyx}^{(2)}$ ,  $\chi_{xyy}^{(2)}$ , and  $\chi_{xyx}^{(2)}$  for symmetric and asymmetric modes.

$360^\circ$ , a polar dependence of the SFG signal in the laboratory frame is obtained that contains information about the different relative contributions  $\chi_{ijk}^{(2)}$ .

Figure 4 shows the calculated polar dependence of the SFG signal for the simulated tensor elements of both the symmetric and asymmetric modes. For the symmetric mode, the  $YYY$  and  $XXY$  elements show a characteristic double-lobed dependence, whereas

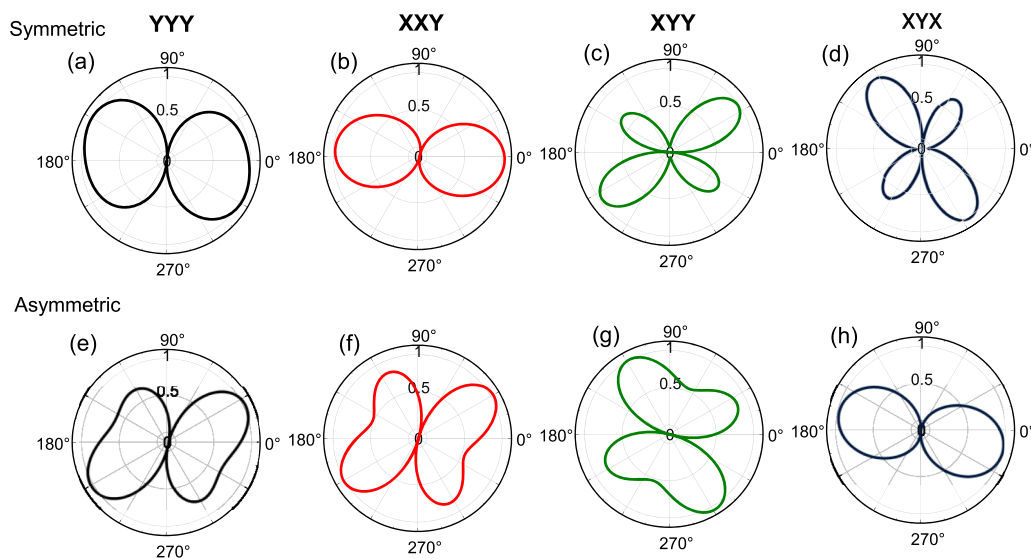


FIG. 4. Simulated polarization-dependence of selected SFG tensor elements for the symmetric and asymmetric stretching modes of methylene in collagen type I. (a)–(d) Simulated results for the symmetric stretch, and (f)–(h) the corresponding response for the asymmetric stretch. The rotation angle  $\Phi$  is defined in Fig. 1(c).

the  $XYX$  and  $XYY$  elements reveal a four-leaf clover pattern. These results mimic the general trends reported in previous polarization-resolved SFG experiments<sup>20,25</sup> but also reveal new asymmetries in the polar profile that are not expected under the common assumption of perfect  $C_\infty$  symmetry. For instance, the  $YYY$  profile does not exhibit mirror symmetry, and the simulated  $XYY$  and  $XYX$  patterns are not strictly identical.

Compared to the symmetric mode, the polar dependence of the contributions from the asymmetric mode reveals markedly different patterns. The  $YYY$  and  $XXY$  elements show a butterfly-like polarization dependence, a pattern that is noticeably distinct from that of the polar response of the symmetric mode. Furthermore, the  $XYY$  plot of the asymmetric vibration also shows a butterfly-like pattern rather than the four-leaf clover profile that was characteristic of the symmetric mode. The same difference is observed in even more striking form for the polar plot of the  $XYX$  measurement. These simulations thus show that the polarization-resolved measurement contains explicit information about the mode symmetry of the driven methylene stretching vibrations.

## B. Spectral dependence of measured SFG tensor elements

We conducted SFG imaging of collagen using our all-reflective SFG collinear microscope. We carefully aligned the long axis of collagen fibrils along the  $Y$ -axis of the laboratory frame to enable a direct comparison with the simulated results. Figure 5 presents the SFG images obtained from the samples of rat tail tendon for the individual SFG tensor elements  $YYY$ ,  $XXY$ ,  $XYY$ , and  $XYX$  when  $\Phi = 0$ . The image contrast obtained from all elements examined here reveals the clear morphological features of aligned collagen fibers. For each of the elements, it can be seen that the SFG signal exhibits a dependence on the frequency of the  $\omega_1$  beam, as evidenced by the differences between the images taken at  $2860\text{ cm}^{-1}$  and  $2942\text{ cm}^{-1}$ .

The spectral dependence of the SFG signal is more clearly displayed in Fig. 6(a), which shows spectra for various tensor elements in the spectral range of the carbon–hydrogen stretching modes. The strongest signals are observed for the  $\chi_{YYY}^{(2)}$  and  $\chi_{XXY}^{(2)}$  tensor elements, which peak near  $2942\text{ cm}^{-1}$ , whereas the signals for the  $\chi_{XYY}^{(2)}$  and  $\chi_{YXY}^{(2)}$  elements are considerably weaker, consistent with findings from prior work.<sup>20</sup> For fibrils aligned along the  $Y$ -axis, we have  $\chi_{IJK}^{(2)} \rightarrow \chi_{ijk}^{(2)}$ , and we find good general correspondence between the magnitude of the SFG signal predicted in the simulations of Fig. 3(a) for the symmetric mode and the signal strength of the various elements measured at  $2942\text{ cm}^{-1}$ . The most significant discrepancy is the higher relative weight of the signal derived from the  $\chi_{XYY}^{(2)}$  and  $\chi_{YXY}^{(2)}$  elements, which appear much weaker in the simulations compared to what is seen in the experiments. Nonetheless, the observed trend in the signal magnitude among the various elements strongly suggests that the SFG signal measured at  $2942\text{ cm}^{-1}$  is dominated by the contributions of the symmetric methylene stretching mode. The spectral result for  $\chi_{XYX}^{(2)}$  is substantially different. While weaker overall compared to the dominant  $\chi_{YYY}^{(2)}$  and  $\chi_{XXY}^{(2)}$  tensor elements,  $\chi_{XYX}^{(2)}$  shows maxima at  $2860$  and  $2917\text{ cm}^{-1}$ . Given that the simulations reveal that  $\chi_{xyx}^{(2)}$  is most sensitive to the

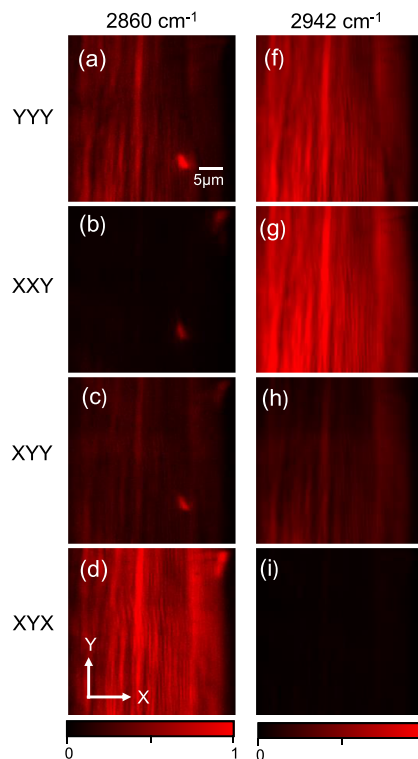


**FIG. 5.** SFG images of collagen in rat tail tendon at different frequencies: (a)–(d)  $2950\text{ cm}^{-1}$  and (f)–(i)  $2860\text{ cm}^{-1}$ . The images are normalized to the maximum  $\chi_{XXY}^{(2)}$  signal at  $2942\text{ cm}^{-1}$  in panel (g), and the values of the first column (a)–(d) are additionally multiplied by a factor of 10. Note that at the lowest SFG signals [panels (a)–(c)], an additional structure becomes visible. This structure is not part of the current analysis.

asymmetric methylene stretching mode, some of the observed maxima may correspond to the resonances of the asymmetric mode. We performed polarization-resolved measurements to investigate this further.

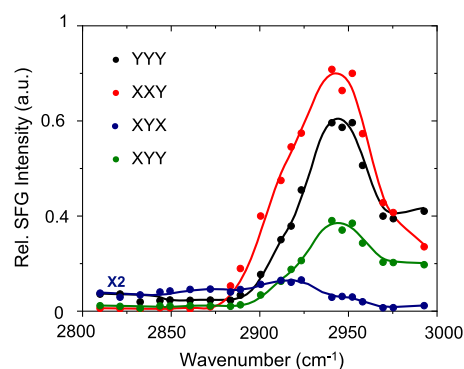


**FIG. 6.** Spectral dependence of tensor elements  $\chi_{YYY}^{(2)}$ ,  $\chi_{XXY}^{(2)}$ ,  $\chi_{XYY}^{(2)}$ , and  $\chi_{YXY}^{(2)}$  in collagen type I when the long axis of collagen is aligned along the  $Y$ -axis ( $\Phi = 0$ ).



### C. Polarization orientation-dependence of measured SFG tensor elements

To examine the dependence of the SFG tensor elements on the polarization orientation of the incident fields, we conducted polarization-resolved SFG measurements of aligned collagen type I fibers. In these measurements, the polarization directions of the  $\omega_1$  and  $\omega_2$  fields were parallel and jointly rotated by the angle  $\Phi$  relative to the Y-axis in the sample plane. The analyzer was rotated by the same angle. Figure 7 presents the  $\Phi$ -dependence of various tensor elements, with the first row and second row corresponding to a vibrational energy of  $2942\text{ cm}^{-1}$  and  $2860\text{ cm}^{-1}$ , respectively. The experimental data points are denoted by dots, while the thick solid lines represent the simulated symmetric and asymmetric angular dependencies of the measured SFG signal for each of the selected elements.

At  $2942\text{ cm}^{-1}$ , the SFG signal in the YYY and XXY configurations exhibits a double-lobed dependence, while the corresponding XYY and XYX signals display a four-leaf pattern. These observations are consistent with the simulations for the symmetric modes of the methylene group. Interestingly, the double-lobe pattern of the YYY configuration aligns along a tilted angle, closely following the simulated results. In all, the polar dependence of all selected elements is in close agreement with the simulated results for the symmetric stretching mode, confirming that the signal measured at  $2942\text{ cm}^{-1}$  is dominated by the symmetric mode. At  $2860\text{ cm}^{-1}$ , the SFG signals for the YYY, XXY, and XYY elements exhibit butterfly-like patterns, whereas the signal observed in the XYX channel displays a double-lobed behavior. For the latter element, the SFG signal shows maxima at  $160^\circ$  and  $340^\circ$ , consistent with the simulated results calculated for the asymmetric methylene stretching mode (Sec. III A). We emphasize that the simulated

results do not represent fits but rather the predicted dependence of the SFG signal based on the position and orientation of the carbon–hydrogen bonds in the crystal structure of collagen type I.

The spectral dependence of the XYX-derived SFG signal is shown separately in Fig. 8, along with the polarization dependence of its main spectral features. Four spectral signatures are singled out here. First, the weak spectral feature near  $2860\text{ cm}^{-1}$  shows a double-lobed polarization dependence, corroborating the pattern expected for an asymmetric  $\text{CH}_2$  vibrational mode. Second, the peak near  $2917\text{ cm}^{-1}$  shows a pattern that resembles a four-leaf clover, showing the features of a symmetric stretching mode in the XYX channel. Third, the signature at  $2942\text{ cm}^{-1}$  also shows a four-lobed pattern, suggesting a symmetric stretching mode. Finally, the weak band near  $3016\text{ cm}^{-1}$  exhibits a double-lobed polarization dependence, reminiscent of an asymmetric mode but with a different tilt angle relative to the profile measured at  $2860\text{ cm}^{-1}$ . To further study the nature of the SFG signal at  $3016\text{ cm}^{-1}$ , we measured the signal in the YYY configuration (shown in S5), revealing a four-lobed pattern that supports the notion that this resonance frequency results from an asymmetric stretching mode.

### D. Vibrational spectra and DFT simulations of amino acid residues

To gain further insights into the origin of the vibrational spectral features observed in the SFG spectrum of collagen type I, we performed DFT calculations on the tripeptide Gly–Pro–Hyp (glycine, proline, and hydroxyproline, respectively), which serves as a model for the repeating unit of the collagen polypeptide chain. In general, the vibrational spectra of tripeptides can differ from those of the actual polypeptide, as vibrational coupling and steric effects in the folded protein can alter vibrational signatures substantially.

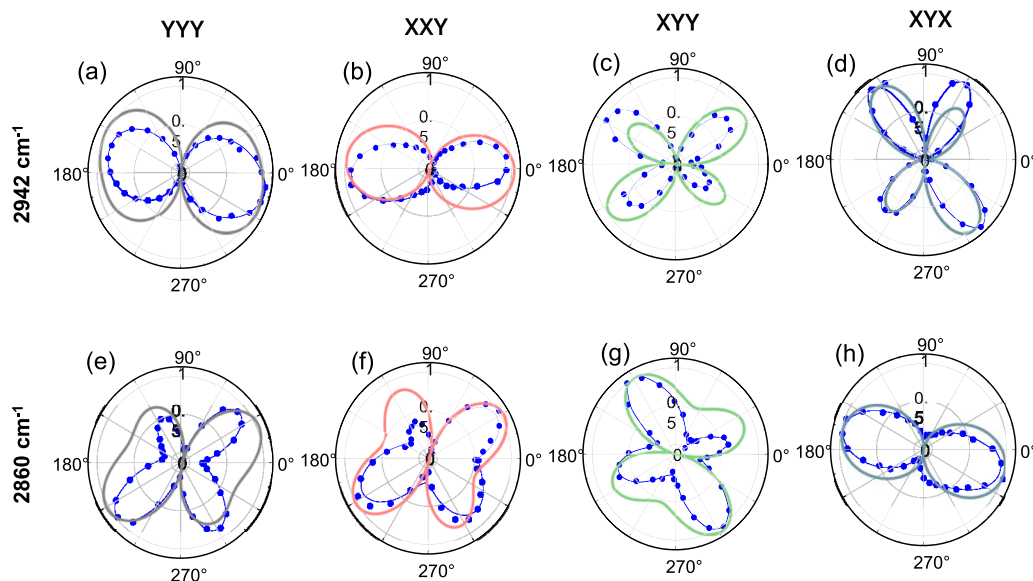


**FIG. 7.** Polarization-orientation ( $\Phi$ ) dependence of selected SFG tensor elements YYY, XXY, XYY, and XYX in collagen type I (rat tail). The top row shows the results obtained at  $2942\text{ cm}^{-1}$ , and the bottom row displays the results obtained at  $2860\text{ cm}^{-1}$ . The dots show the experimental data points in blue, and the thick solid lines show the simulated results based on the crystal structure of collagen type I.

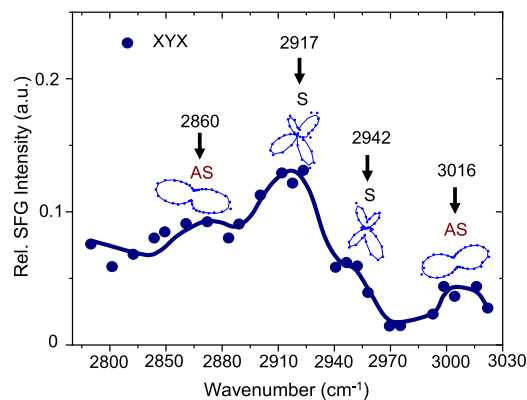


**FIG. 8.** Spectral and polarization dependencies of the SFG signal in the XYX channel, with polarization plots presented at the frequencies 2860, 2917, 2942, and 3016  $\text{cm}^{-1}$ . The fibrillar axis is aligned along the laboratory Y-axis ( $\Phi = 0$ ). The dots show the experimental data points, whereas the thick solid line is a guide to the eye. The spectra are normalized to the maximum  $\chi_{\text{XXY}}^{(2)}$  signal in Fig. 6.

Nonetheless, the DFT predicted Raman- and IR-active modes of the tripeptide provide a first-order impression of methylene resonances in fibrillar collagen that can be used to refine the assignment of the SFG spectral features.

The calculated Raman- and IR-active modes of the tripeptide are shown in Figs. 9(a) and 9(b), respectively, along with the measured vibrational spectra of collagen in rat tail tendon. The calculated modes fall into two main categories: (i) symmetric ( $\sim 2880 \text{ cm}^{-1}$ ) and asymmetric ( $\sim 2980 \text{ cm}^{-1}$ ) stretching mode of the glycine methylene group, and (ii) symmetric ( $2940\text{--}3010 \text{ cm}^{-1}$ )

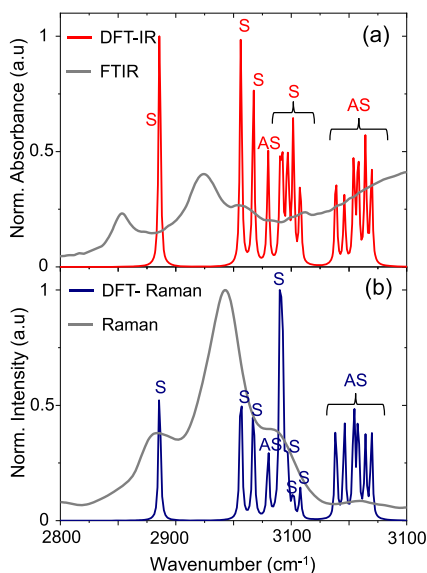


**FIG. 9.** IR absorption (a) and Raman (b) modes of Gly-Pro-Hyp as predicted by DFT calculations. The gray solid lines indicate the experimental vibrational spectra of collagen in rat tail tendon. S and AS indicate the symmetric and asymmetric modes, respectively.

**TABLE I.** Wavenumbers and band assignments for collagen type I using SFG.

	2860 $\text{cm}^{-1}$	2917 $\text{cm}^{-1}$	2942 $\text{cm}^{-1}$	3016 $\text{cm}^{-1}$
YYY	$v_{as} \text{ CH}_2$	...	$v_s \text{ CH}_2$	$v_{as} \text{ CH}_2$
XXY	$v_{as} \text{ CH}_2$	...	$v_s \text{ CH}_2$	...
YXY	$v_{as} \text{ CH}_2$	...	$v_s \text{ CH}_2$	...
XYX	$v_{as} \text{ CH}_2$	$v_s \text{ CH}_2$	$v_s \text{ CH}_2$	$v_{as} \text{ CH}_2$

and asymmetric ( $3030\text{--}3080 \text{ cm}^{-1}$ ) stretching modes of methylene groups on the proline and hydroxyproline rings. The lowest vibrational energies are observed for the single methylene group of Gly, whereas the  $\text{CH}_2$  oscillators on the pyrrolidine rings show a high degree of intra-ring coupling, which appears to blueshift both the symmetric and asymmetric mode vibrations. The DFT-derived assignments are summarized in Table S1 of the supplementary material.

The comparison with the measured collagen spectra reveals that the resonances predicted by DFT exhibit an overall blueshift relative to what is experimentally observed (resonance frequencies are not rescaled in this study). We note that the DFT simulations of the tripeptide are performed in the gas phase, which may partially account for the spectral shifts of the resonance frequencies relative to those observed in the experiment. Nonetheless, the trends revealed by the DFT calculations provide important clues that can be used for guiding the assignment of the observed SFG spectral features. Based on these trends, we assign the weak spectral SFG feature at  $2860 \text{ cm}^{-1}$  to the asymmetric  $\text{CH}_2$  mode of glycine. Although the lowest frequency asymmetric methylene stretching mode predicted by the DFT simulations is significantly blueshifted from the mode observed at  $2860 \text{ cm}^{-1}$ , the asymmetric glycine mode remains the most probable candidate that exhibits the correct symmetry properties. It is possible that vibrational coupling effects in the three-dimensional collagen type I structure, which are not included in the DFT simulations, account for the experimentally observed redshift of this mode. The spectral signatures near  $2917 \text{ cm}^{-1}$  are attributed to the symmetric stretches of Pro-methylene groups, and the main peak at  $2942 \text{ cm}^{-1}$  is assigned to symmetric stretches on both Pro and Hyp residues. Finally, the signatures between  $2980 \text{ cm}^{-1}$  and  $3030 \text{ cm}^{-1}$  are assigned to the asymmetric stretching vibrations of the Pro and Hyp methylene groups (Table I).

#### IV. DISCUSSION

In this work, we performed detailed measurements and simulations to reveal the nature of the spectral features of the SFG signal derived from collagen type I in the CH-stretching vibrational range. To enable a direct measurement of individual tensor elements of collagen's second-order susceptibility, we carried out experiments in an optimized all-reflective laser-scanning SFG microscope. This experimental strategy allows for a careful inspection of the overall alignment of collagen fibers at the microscopic scale, which, compared to macroscopic measurements, improves confidence in aligning the reference frame of the triple-helix structure of collagen with the laboratory frame. In addition, the excellent achromatic

and polarization properties of the all-reflective imaging system permit accurate polarization-resolved SFG measurements, resulting in a dataset that allows for a comparison of the magnitude and spectral response among selected tensor elements.

To analyze the data, we used the 3D atomic positions extracted from the crystal structure of fibrillar collagen to determine the expected  $\chi_{ijk}^{(2)}$  response of its triple helix structure. This approach goes beyond models that assume cylindrical symmetry for fibrillar collagen, as it takes the actual position and orientation of the contributing vibrational oscillators into account. For instance, compared to computations based on  $C_\infty$  symmetry, our simulations predict finite values for tensor elements that would otherwise vanish based on cylindrical symmetry. Instead, such elements contribute in a meaningful way and affect, for instance, the polarization dependence of the SFG signal. As an example, the tilt angle of the double-lobe polarization dependent profile seen for the  $\chi_{XXY}^{(2)}$  measurement at  $2942\text{ cm}^{-1}$  is faithfully reproduced in the simulations, a feature not seen in calculations based on  $C_\infty$  symmetry. Similarly, all qualitative features of the butterfly-type and four-leaf clover patterns, observed in the measurements, are correctly predicted by the simulations, including the proper tilt angles of the profiles.

At the same time, there are some features in the experimental polar plots that are not reproduced in the simulations. In particular, the more indented butterfly pattern observed in the experiments is not predicted by the simulated results. A possible reason for such discrepancies is the notion that the simulations are based on a relatively short segment of the collagen molecule, whereas the actual sample not only contains longer segments, but also the complete hierarchical structure of fibrous collagen that is not considered in the simulations. The molecular segment considered also contains 74 single C–H bond oscillators, although our simulated data suggest that its predicted features do not show up in the experimental results; see Sec. S4 of the supplementary material. Furthermore, it is possible that methyl groups, though sparse in the collagen structure, contribute nonetheless to the measured SFG signal. Despite these considerations, the palpable similarity between the experimental results and the simulated signal, both in terms of the relative magnitude of the tensor elements as well as their polarization dependence, fosters confidence that the assumptions made are reasonable and that the interpretation of the data is likely meaningful.

Our analysis reveals that the dominant spectral feature in the SFG spectrum at  $2942\text{ cm}^{-1}$  can be attributed with confidence to a symmetric stretching mode of methylene. This finding is in agreement with previous assignments.<sup>20,25</sup> However, our DFT calculations suggest that these resonances can be assigned to the fundamental modes of methylene groups on the Pro and Hyp pyrrolidine rings and that Fermi-shifted resonances are not required to explain the relatively high energy of the methylene stretches involved. Instead, the blueshift appears to be the result of intra-ring coupling of methylene modes in the somewhat strained pyrrolidine rings (the intra-ring carbon  $sp^3$  bond angle is  $111.6^\circ$ ). Similar observations have been made in the SFG measurements of crystalline cellulose,<sup>38,39</sup> which also exhibits symmetric methylene stretching resonances in the  $2900\text{--}3000\text{ cm}^{-1}$  range that have a highly delocalized character. Unlike previous work, we also find evidence of asymmetric methylene modes in the SFG spectrum, including the spectral features in the  $2850\text{--}2870\text{ cm}^{-1}$  range, assigned to glycine,

and the spectral region near  $2980\text{--}3030\text{ cm}^{-1}$ , attributed to Pro and Hyp. Overall, the SFG spectrum is dominated by symmetric stretching modes, whereas the asymmetric modes only weakly contribute to the detected SFG response.

## V. CONCLUSION

In this work, we studied the vibrational spectral SFG features of collagen type I. Making use of an all-reflective SFG microscope and utilizing the atomic data derived from the crystal structure of fibrillar collagen, we identified the mode symmetry of the main SFG signatures in the CH-stretching vibrational range and provided assignments based on the contribution of collagen's main amino acid residues. These assignments were facilitated by the ability to perform accurate polarization-resolved measurements of individual tensor elements of the sample's second-order susceptibility. We attribute the dominant spectral feature of the SFG spectrum at  $2942\text{ cm}^{-1}$  to the symmetric methylene stretches of the Pro and Hyp residues. The involvement of possible Fermi resonances is not essential for explaining their peak positions. We also found evidence of asymmetric methylene stretching modes in the targeted spectral range, albeit the latter modes contribute only weakly to the SFG spectrum. The results in this study underline the utility of the polarization-resolved SFG microscope and help establish the relationship between SFG spectral signatures and the structural properties of protein assemblies in biological specimens.

## SUPPLEMENTARY MATERIAL

The supplementary material includes information about the rotation matrices used in this work, their use to compute the nonlinear susceptibilities, a numerical representation of the nonlinear susceptibility tensor for collagen type I, and a complete list of DFT-derived mode assignments.

## ACKNOWLEDGMENTS

This work was funded by the National Institutes of Health, Grant No. R01-GM132506.

## AUTHOR DECLARATIONS

### Conflict of Interest

The authors have no conflicts to disclose.

## Author Contributions

**Yryx Y. Luna Palacios:** Data curation (lead); Formal analysis (lead); Investigation (lead); Software (equal); Visualization (lead); Writing – original draft (lead). **Salile Khandani:** Investigation (equal). **Evan P. Garcia:** Investigation (supporting). **Anabel Chen:** Investigation (supporting). **Siyang Wang:** Formal analysis (equal); Software (equal). **Khokan Roy:** Investigation (supporting). **David Knez:** Methodology (lead); Software (equal). **Do A. Kim:** Methodology

(equal); Software (supporting). **Israel Rocha-Mendoza**: Conceptualization (equal); Supervision (equal); Validation (equal); Writing – review & editing (equal). **Eric O. Potma**: Conceptualization (equal); Data curation (equal); Funding acquisition (lead); Project administration (lead); Resources (lead); Supervision (lead); Validation (lead); Visualization (equal); Writing – review & editing (equal).

## DATA AVAILABILITY

The data that support the findings of this study are available from the corresponding author upon reasonable request.

## REFERENCES

- <sup>1</sup>B. Brodsky and J. A. M. Ramshaw, *Matrix Biol.* **15**(8-9), 545 (1997).
- <sup>2</sup>A. Aparecida de Aro, B. de Campos Vidal, and E. R. Pimentel, *Micron* **43**(2-3), 205 (2012).
- <sup>3</sup>P. J. Campagnola and C. Y. Dong, *Laser Photonics Rev.* **5**(1), 13 (2011).
- <sup>4</sup>X. Chen, O. Nadiarynkh, S. Plotnikov, and P. J. Campagnola, *Nat. Protoc.* **7**(4), 654 (2012).
- <sup>5</sup>R. Cicchi, N. Vogler, D. Kapsokalyvas, B. Dietzek, J. Popp, and F. S. Pavone, *J. Biophot.* **6**(2), 129 (2013).
- <sup>6</sup>R. Mercatelli, F. Ratto, F. Rossi, F. Tatini, L. Menabuoni, A. Malandrini, R. Nicoletti, R. Pini, F. S. Pavone, and R. Cicchi, *J. Biophot.* **10**(1), 75 (2017).
- <sup>7</sup>T. Y. Lau, R. Ambekar, and K. C. Toussaint, *Opt. Express* **20**(19), 21821 (2012).
- <sup>8</sup>M. Rivard, K. Popov, C. A. Couture, M. Laliberté, A. Bertrand-Grenier, F. Martin, H. Pépin, C. P. Pfeffer, C. Brown, L. Ramunno, and F. Légaré, *J. Biophot.* **7**(8), 638 (2014).
- <sup>9</sup>C. A. Couture, S. Bancelin, J. Van der Kolk, K. Popov, M. Rivard, K. Légaré, G. Martel, H. Richard, C. Brown, S. Laverty, L. Ramunno, and F. Légaré, *Biophys. J.* **109**(12), 2501 (2015).
- <sup>10</sup>P. J. Su, W. L. Chen, Y. F. Chen, and C. Y. Dong, *Biophys. J.* **100**(8), 2053 (2011).
- <sup>11</sup>F. Tiaho, G. Recher, and D. Rouède, *Opt. Express* **15**(19), 12286 (2007).
- <sup>12</sup>A. E. Tuer, S. Krouglov, N. Prent, R. Cisek, D. Sandkuijl, K. Yasufuku, B. C. Wilson, and V. Barzda, *J. Phys. Chem. B* **115**(44), 12759 (2011).
- <sup>13</sup>M. Kröger, J. Schleusener, S. Jung, and M. E. Darwin, *Photonics* **8**, 404 (2021).
- <sup>14</sup>T. Hompland, A. Erikson, M. Lindgren, T. Lindmo, and C. de Lange Davies, *J. Biomed. Opt.* **13**(5), 054050 (2008).
- <sup>15</sup>J. Y. Huang and Y. R. Shen, *Laser Spectroscopy and Photochemistry on Metal Surfaces* (World Scientific, 1995), Vol. 1, p. 5.
- <sup>16</sup>Y. R. Shen, *Nature* **337**(6207), 519 (1989).
- <sup>17</sup>A. Hanninen, M. W. Shu, and E. O. Potma, *Biomed. Opt. Express* **8**(9), 4230 (2017).
- <sup>18</sup>V. Raghunathan, Y. Han, O. Korth, N. H. Ge, and E. O. Potma, *Opt. Lett.* **36**(19), 3891 (2011).
- <sup>19</sup>H. F. Wang and W. Xiong, *Annu. Rev. Phys. Chem.* **72**, 279 (2021).
- <sup>20</sup>Y. Han, J. Hsu, N. H. Ge, and E. O. Potma, *J. Phys. Chem. B* **119**(8), 3356 (2015).
- <sup>21</sup>Y. Han, V. Raghunathan, R. Feng, H. Maekawa, C. Y. Chung, Y. Feng, E. O. Potma, and N. H. Ge, *J. Phys. Chem. B* **117**(20), 6149 (2013).
- <sup>22</sup>H. Maekawa, S. K. K. Kumar, S. S. Mukherjee, and N.-H. Ge, *J. Phys. Chem. B* **125**(33), 9507 (2021).
- <sup>23</sup>P. K. Johansson and D. G. Castner, *Langmuir* **35**(24), 7848 (2019).
- <sup>24</sup>P. K. Johansson and P. Koelsch, *J. Am. Chem. Soc.* **136**(39), 13598 (2014).
- <sup>25</sup>I. Rocha-Mendoza, D. R. Yankelevich, M. Wang, K. M. Reiser, C. W. Frank, and A. Knoesen, *Biophys. J.* **93**(12), 4433 (2007).
- <sup>26</sup>Y. Zhu, X. Yang, and F. Sun, Protein data bank (2023).
- <sup>27</sup>H. F. Wang, W. Gan, R. Lu, Y. Rao, and B. H. Wu, *Int. Rev. Phys. Chem.* **24**(2), 191 (2005).
- <sup>28</sup>J. Choi, A. L. Kwansa, Y. G. Yingling, and S. H. Kim, *J. Phys. Chem. B* **127**(39), 8456 (2023).
- <sup>29</sup>C. Hirose, N. Akamatsu, and K. Domen, *J. Chem. Phys.* **96**(2), 997 (1992).
- <sup>30</sup>C. Hirose, H. Yamamoto, N. Akamatsu, and K. Domen, *J. Phys. Chem.* **97**(39), 10064 (1993).
- <sup>31</sup>X. Wei, S. C. Hong, X. Zhuang, T. Goto, and Y. R. Shen, *Phys. Rev. E* **62**(4), 5160 (2000).
- <sup>32</sup>S. V. Plotnikov, A. C. Millard, P. J. Campagnola, and W. A. Mohler, *Biophys. J.* **90**(2), 693 (2006).
- <sup>33</sup>J. M. Perry, A. J. Moad, N. J. Begue, R. D. Wampler, and G. J. Simpson, *J. Phys. Chem. B* **109**(42), 20009 (2005).
- <sup>34</sup>G. J. Simpson, *ChemPhysChem* **5**(9), 1301 (2004).
- <sup>35</sup>G. J. Simpson, *Nonlinear Optical Polarization Analysis in Chemistry and Biology* (Cambridge University Press, Cambridge, UK, 2017).
- <sup>36</sup>A. Erikson, J. Örtengren, T. Hompland, C. de Lange Davies, and M. Lindgren, *J. Biomed. Opt.* **12**(4), 044002 (2007).
- <sup>37</sup>P. Stoller, P. M. Celliers, K. M. Reiser, and A. M. Rubenchik, *Appl. Opt.* **42**(25), 5209 (2003).
- <sup>38</sup>C. M. Lee, X. Chen, P. A. Weiss, L. Jensen, and S. H. Kim, *J. Phys. Chem. Lett.* **8**(1), 55 (2017).
- <sup>39</sup>X. Chen, C. M. Lee, H.-F. Wang, L. Jensen, and S. H. Kim, *J. Phys. Chem. C* **121**(34), 18876 (2017).